Organic Electronics 13 (2012) 1100–1104

Contents lists available at SciVerse ScienceDirect

Organic Electronics

journal homepage: www.elsevier.com/locate/orgel

Revealing nanoscale phase separation in small-molecule photovoltaic blends by plasmonic contrast in the TEM

Wolfram Schindler *, Markus Wollgarten, Konstantinos Fostiropoulos

Helmholtz-Zentrum Berlin für Materialien und Energie GmbH, Hahn-Meitner-Platz 1, 14109 Berlin, Germany

ARTICLE INFO

Article history:
Received 7 January 2012
Received in revised form 8 March 2012
Accepted 8 March 2012
Available online 22 March 2012

Keywords:
Organic bulk heterojunction solar cell
Phase separation
Electron energy loss spectroscopy
TEM spectrum imaging

ABSTRACT

Good prospects of organic solar cells (OSC) are dampened by relatively poor transport properties in the organic donor–acceptor (D–A) absorber system. A widely recognized key to overcome this drawback is the ability to control its D–A morphology at the bulk heterojunction (BHJ) on the nanometer scale. An essential prerequisite for this is to characterize the BHJ of the carbonaceous materials combination. However, due to their similarity, particularly if not crystalline, only poor-contrast images are achieved by conventional transmission electron microscopy (TEM).

We apply energy filtered transmission electron microscopy spectrum imaging (EFTEM SI) to study local phase separation with chemical sensitivity in a co-evaporated zinc phthalocyanine (ZnPc) (D) and C_{60} (A) blend layer. As image contrast we exploit the significant difference between the plasmon energies of the pure materials (23 and 26 eV for ZnPc and C_{60}, respectively) as recorded by electron energy loss spectroscopy.

In order to fully understand its structure and morphology, on the one hand conventional TEM analysis allows to identify suitably oriented crystalline phases on the basis of lattice fringes (here only C_{60}). On the other hand the EFTEM SI plasmon map discloses the complete lateral distribution of the two molecular phases independent of crystallinity.

1. Introduction

1.1. Materials

Organic solar cells (OSCs) have gained great attention because of promising diversity, low-cost production on flexible substrates and considerable increase of power-conversion efficiencies (PCEs) during the last decade. State-of-the-art devices reach PCEs higher than 8% on technological relevant areas of more than 1 cm^2 as reported for a donor–acceptor (D–A) heterojunction based on small molecular weight materials and similar for polymer based light absorbers [1]. A key parameter for high PCEs is a well-defined morphology of the D–A blend which provides both optimized charge carrier generation at the D–A interface and charge transport to the electrodes. Thus the challenge is the growth of crystalline percolating D–A networks which are entangled on the nanometer scale, i.e. in the range of the exciton diffusion length. Blend films of small molecules, like the prominent pair C_{60} and zinc or copper phthalocyanine (ZnPc or CuPc), are advantageous for preparation since physical vapor deposition enables an accurate control of process parameters like deposition rate, thickness, mixing ratio and substrate temperature. Recently we have reported on temperature induced phase separation in phthalocyanine:C_{60} bulk heterojunction (BHJ) layers [2–4]. We attributed the improvement of device parameters to an optimized D–A interface morphology in accordance with similar preceding reports [5–7]. To understand the demixing process in all stages of fabrication

* Corresponding author. Tel.: +49 30 8062 42159; fax: +49 30 8062 43199.
E-mail addresses: wolfram.schindler@helmholtz-berlin.de (W. Schindler), wollgarten@helmholtz-berlin.de (M. Wollgarten), fostiropoulos@helmholtz-berlin.de (K. Fostiropoulos).

1566-1199/$ - see front matter © 2012 Elsevier B.V. All rights reserved.
http://dx.doi.org/10.1016/j.orgel.2012.03.008

there is substantial need for techniques that can resolve the distribution of the different carbonaceous components with chemical sensitivity on the nanoscale.

1.2. Electron microscopy spectrum imaging

Mainly conventional transmission electron microscopy (TEM) methods have been used to image aggregation in organic BHJ on the nanoscale besides X-ray microscopy [8] as well as surface sensitive techniques like atomic force microscopy (AFM) or Kelvin probe force microscopy [2,9,10]. TEM tomography has been successfully applied on few polymer/C_{60} derivate blends for which sufficient differences in electron density or diffraction contrast exist [11,12]. Particularly in small-molecular-weight blends conventional TEM is applicable to map materials with sub-10 nm resolution by their characteristic lattices [13] but this approach is limited to crystalline phases adequately orientated to the incident beam.

Without these restrictions, energy filtered TEM spectrum imaging (EFTEM SI) on basis of distinctive electron energy loss spectra is a potential mapping technique for blends of akin carbonaceous species. Hunt et al. [14] have first demonstrated that for a two-phase polymer chemical contrast imaging on basis of the π–π^* transition is suitable, which occurs close to the zero-loss peak (ZLP) at energy-loss of about 6 eV in graphitic carbon. The $(\sigma + \pi)$ plasmon excitation of the valence electrons exhibits the highest intensity apart from the ZLP as depicted in Fig. 1 and varies from ~22 to 33 eV for different forms of carbon [15,16]. Therefore, use of the $(\sigma + \pi)$ plasmon is naturally predisposed to map the distribution of carbonaceous materials as Gass et al. [17] have shown for spectral tomography of a multiwalled carbon nanotube dispersed in nylon. Only recently, the same spectral feature has been employed to image the phase separation in a BHJ consisting of the polymer P3HT and fullerene-derivative PCMB [18,19]. At high energy-loss, information about present elements as well as molecular structure and orientation can be gained at the ionization edges [20]. However, the signal intensity in this range is about 100 times lower than in the $(\sigma + \pi)$ plasmon regime at low energy-loss.

In our study on the material combination ZnPc and C_{60} we focused on the most intense distinctive feature, the $(\sigma + \pi)$ plasmon, to allow for a clear distinction from background. First, the shift of the plasmon position as a function of the ZnPc:C_{60} mixing ratio was investigated by electron energy loss spectroscopy (EELS). On the basis of these reference spectra we applied spectrum imaging to analyze the local phase separation in realistic ZnPc:C_{60} OSC absorber layers.

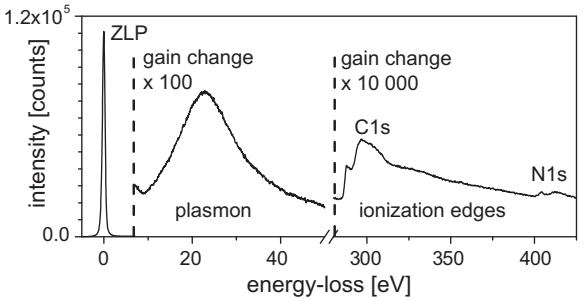

Fig. 1. Electron energy-loss spectrum of a 40 nm thick zinc phthalocyanine layer. The plasmon peak height is the order of hundred smaller than the zero-loss peak (ZLP) height. The intensity of the carbon ionization edge is again two orders of magnitude lower than that of the plasmon.

2. Experimental methods

2.1. Sample preparation

Single layers, bilayers and blend layers composed of ZnPc and C_{60} were prepared by evaporation under high vacuum conditions (<1×10^{-7} mbar) on cleaved mica substrates with deposition rates of 0.5–1 Å/s. Thicknesses were carefully controlled using individual quartz crystal sensors (Inficon IC/5 monitor) which were calibrated by X-ray reflectivity measurements. The blend layers were grown by simultaneously depositing ZnPc and C_{60}. For recording single electron energy loss spectra, samples with total thicknesses of 40 nm were prepared at room temperature (25 °C). For spectrum imaging a 80 nm thick blend layer was deposited which represents the typical absorber thickness in ZnPc:C_{60} BHJ solar cells. This layer was grown on a substrate heated to 90 °C which is known to yield improved device performance compared to deposition at room temperature [3,6,7]. All films were floated-off in water and transferred on standard TEM grids (400 mesh) without using additional support films.

2.2. Electron microscopy

TEM experiments were performed using a Zeiss LIBRA 200 microscope operated at 200 kV. The microscope is equipped with a field emission gun and a high resolution in-column energy-filter. In EELS mode, this system yields energy resolution values of <0.7 eV. All investigations were conducted without the use of an objective aperture. EELS spectra were captured from circular sample areas of 300 nm in diameter defined by the filter entrance aperture. The spectra were recorded with 163-fold spectrum magnification, 0.1 s acquisition time, summed over 10 reads and with full CCD resolution corresponding to 0.04 eV/pixel. Plasmon peak centers were determined by an automatic Gaussian fitting routine. To gain higher precision, all center positions were estimated first by a fitting in the fixed energy interval from 20 to 30 eV followed by a second fitting in a 6 eV region around the initially approximated values.

To map the plasmon position a data cube was acquired by EFTEM SI [21]. A series of energy filtered images was recorded in the region from 15 to 35 eV using a 1.7 eV window and an energy increment of 0.8 eV. Here the window width limits the energy resolution. Images of 367×367 nm were taken with 4× CCD binning, i.e. 512×512 pixels, summed over 4 reads with an acquisition time of 3 s each. The electron dose of one image was roughly 2×10^6 e^-/nm^2, which is much lower than electron doses required for employing ionization edge contrast. In order to correct distortions of the data cube,

additional measures were taken. For spatial shift correction, several reference images at zero energy-loss were taken during the acquisition [22]. To measure energy drift and non-isochromaticity, i.e. energy deviation towards the image corners with respect to the image center, the ZLP positions across the image area were each mapped before and after plasmon image stack acquisition. Interpolation between the first and second ZLP map gives the actual energy drift of the image. Plasmon spectra were extracted pixel-by-pixel from the spatially aligned and further 2× binned image stack (i.e. 1.4 nm/pixel). Their energy axes were adjusted according to the correction function calculated from the (smoothened) ZLP maps. In each spectrum the center of the plasmon peak was determined in the same way as for the single EELS spectra.

3. Results and discussion

3.1. Electron energy loss spectroscopy

EELS spectra of 40 nm thick layers of pure ZnPc, pure C_{60} and their blends are displayed in Fig. 2. All spectra are normalized to exhibit equal integrals in the measured range from −5 to 65 eV. The peak at 7 eV is related to a π–π^* transition [23] and rises with the C_{60} fraction. The major feature in the low-loss region is the plasmon centered at 23 eV for pure ZnPc [24] and near 26 eV for pure C_{60} [23,25,26], respectively. The C_{60} spectrum between 9 and 40 eV has a 13% higher integral than the ZnPc peak and exhibits several additional shoulders originating from interband transitions [23]. In contrast, the ZnPc layer exhibits a featureless peak shape. When the C_{60} fraction is increased the plasmon peak of the blend layer transforms from the ZnPc shape to that of pure C_{60}.

In order to prove that the plasmon peak is not affected by possible radiation damage during the EFTEM SI measurement of the blend, EELS spectra before and after are compared. As a result, the plasmon curves turn out to be consistent. However, the intensity of the π^* feature of the blend at 7 eV decreased as expected indicating radiation damage to the conjugated system [14,27]. Note that the pure ZnPc sample (Fig. 2, dark blue curve) hardly shows any feature in the π^* range. We suppose that this effect is due to the acceleration voltage of $V = 200$ kV damaging rapidly the ZnPc π-system in our measurements as opposed to Flatz et al. [24] where a distinct feature is reported for $V = 100$ kV.

Fig. 3 shows the relation between the plasmon position and the layer composition for three data sets in more detail. The first data set displays peak centers extracted from computed superpositions of the ZnPc and C_{60} prototype spectra (depicted as a black line). This line is curved due to the unequal prototype peak shapes. The second data set is obtained from EELS spectra that were taken for a series of C_{60}/ZnPc bilayer samples with thickness pairs of 10 nm/30 nm, 20 nm/20 nm and 30 nm/10 nm, respectively (shown as diamonds). The third data set plotted as triangles and their dashed trend line are the plasmon positions of 40 nm thick blend layers which were prepared with the same C_{60}:ZnPc ratios as used for the bilayer measurements as well as an additional sample with a 35 nm:5 nm ratio. Each specimen was measured at several locations. Within ±0.1 eV deviation all (except one ZnPc outlier) position values of the same sample were constant.

While the plasmon positions of the bilayer samples clearly coincide with the theoretically derived values, the respective blend samples apparently exhibit lower values. This difference can be explained assuming that the C_{60} EELS spectra differ depending on whether the molecules are isolated (or form small agglomerates) in the blend or build a compact extended ("bulk") film in the bilayer. Keller and Coplan [28] reported the absence of the peak at 26 eV in the gas phase spectrum of C_{60} which is present in EELS spectra of solid films. A characteristic photoemission peak at 28 eV was also absent in C_{60} films of up to two molecular mono-layers [29]. To our knowledge,

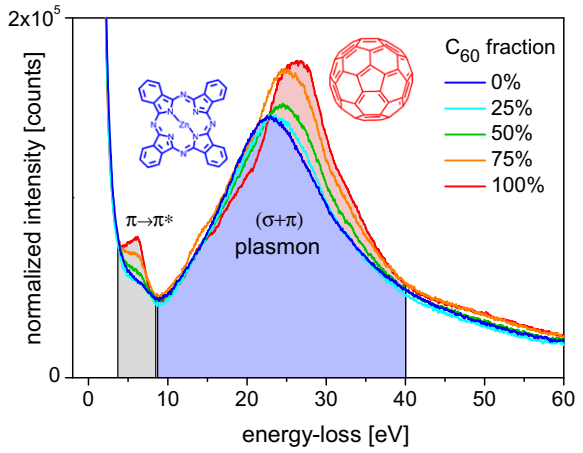

Fig. 2. EELS of 40 nm thick layers of pure ZnPc (blue), pure C_{60} (red) and their blends. The position of the ($\sigma + \pi$) plasmon shifts with increasing C_{60} fraction. Spectra are normalized to have equal integrals between −5 and 65 eV. (For interpretation of the references to color in this figure legend, the reader is referred to the web version of this article.)

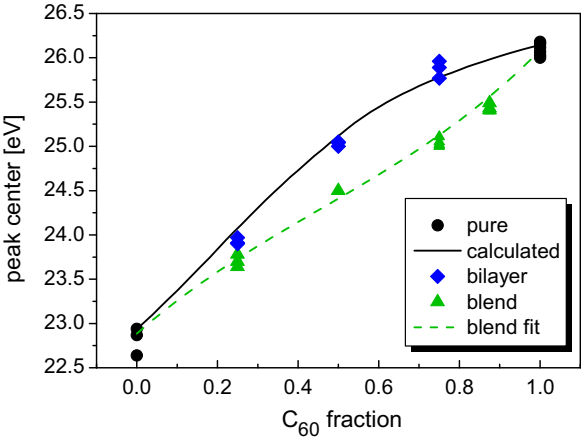

Fig. 3. Plasmon peak centers as function of C_{60} fraction. Data of the pure ZnPc and C_{60} layers are represented as circles. The superpositions of the pure spectra are plotted as solid curve which agrees with the experimental bilayer values (diamonds). Plasmon positions of the respective blends (triangles) are lower. A 3rd order polynomial fit to the blend values is indicated as dashed line.

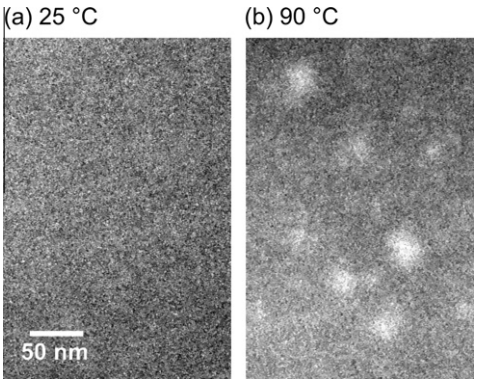

Fig. 4. Energy filtered TEM images collected at 25.4 eV energy-loss. (a) The image of a 40 nm thick ZnPc:C_{60} blend deposited on a substrate at 25 °C is featureless. (b) A 80 nm thick blend deposited at 90 °C reveals bright domains presumably indicating agglomeration. In both images gray scales are adjusted to display deviations of ±15% of the respective image mean value. The gradients are due to non-isochromaticity.

similar effects for phthalocyanines are not reported. The plasmon excitations might be further influenced by different coupling between like and unlike molecules.

The difference in plasmon peak position for bilayer and blend sample at identical composition ratios demonstrates that mixing effects clearly affect the plasmon spectrum of the blend films and cannot be simply neglected. Though the relation between blend composition and plasmon position is empiric, a fitted calibration curve allows for determining unknown mixing ratios in blend films.

3.2. Energy filtered transmission electron microscopy spectrum imaging

Phase separation of ZnPc and C_{60} in the blend was investigated by EFTEM SI. A series of energy filtered images at specific electron energy-losses in the plasmon range was recorded for the 1:1 (thickness ratio) blend deposited at 25 °C. However, as exemplarily shown for the image taken at 25.4 eV (Fig. 4a), all images are featureless indicating a homogeneous layer thickness and good intermixing of the two constituents which agrees with previous conventional TEM studies [3,13]. A second EFTEM SI experiment was performed on a 80 nm thick blend layer (1:1 molar) deposited at elevated substrate temperature of 90 °C as was used for the absorber in OSC devices in a previous study [3]. Fig. 4b displays the image collected at 25.4 eV energy-loss. This intensity image clearly reveals differences in the absorption cross section. Bright domains presumably indicate agglomerations but the chemistry cannot be differentiated. Only the plasmon position map which was extracted from the whole image stack establishes the basis for an unambiguous interpretation (Fig. 5a). The mapped plasmon energies range between 24.3 and 25.4 eV representing the local molecular mixing ratios averaged over the layer thickness. Correlation with the reference spectra presented in the previous section allows to readily identify C_{60} domains. However, determination of the local layer composition faces some difficulties. We expect the spectroscopic behavior of this partially phase separated blend to be a combination of bilayer and blend which have different relations between composition and plasmon peak as demonstrated in the preceding section. Thus, the accuracy of the calibration is limited by the horizontal difference of their respective curves in Fig. 3.

Numerous of domains can be observed with sizes of up to 25 nm in the plasmon map. This is supported by the conventional TEM micrograph of the same spot (Fig. 5b). Domains which are identified as C_{60} due to its characteristic lattice [13] like in selection B also emerge in the plasmon map as C_{60} – rich domains but not vice versa as selection A is an example. Even most of the light areas in Fig. 5b show faint C_{60} lattice fringes indicating that pure C_{60} is outside the large domains as well and presumably interconnects them. The gray value of some of the dark spots in the TEM image can be related to the C_{60} content but a number of contrast effects with fundamentally different origins exist. Often, diffraction contrast rules the conventional TEM image. Contrary to this, plasmon mapping was shown to be insensitive to the orientation of a graphite crystal [16].

While both techniques indicate the presence of C_{60} agglomerates no ZnPc agglomerations in the blend are detected by either method. However, ZnPc can hardly be

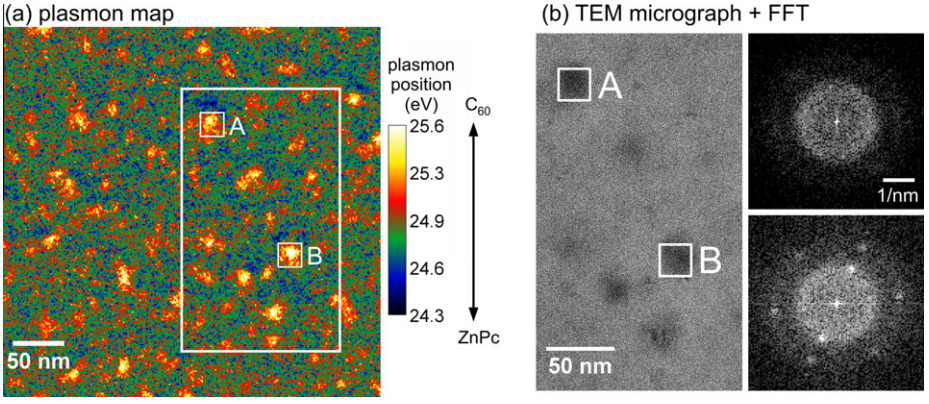

Fig. 5. (a) Plasmon position map showing the phase separation in a 80 nm thick ZnPc:C_{60} blend (1:1) deposited at 90 °C substrate temperature. Two domains A and B are indicated which both appear C_{60}-rich. (b) TEM micrograph (zero-loss filtered) of the same outlined location gives lattice information only for domain B as illustrated by fast Fourier transformation (FFT) indicating diffraction pattern of the C_{60} [1 1 1] zone.

assessed by observation of lattice fringes in conventional TEM. Crystalline reflections of the pure ZnPc sample vanished rapidly in the beam whereas C_{60} domains showed crystalline reflections even after the EFTEM SI acquisition. Hence, only the plasmon map proves the absence of distinct ZnPc agglomerates and verifies that agglomeration of C_{60} is more likely than that of ZnPc [3].

4. Conclusions

The plasmon map obtained for the ZnPc:C_{60} blend layer deposited at 90 °C substrate temperature clearly reveals the temperature induced phase separation of the two components. Thus our TEM investigations confirm the improvement of the D–A morphology to which recent reports attributed enhanced device performance when depositing the phthalocyanine:C_{60} blend layer on a heated substrate [2–7]. Demixing of the blend forms shorter charge carrier percolation paths while excitons in the 25 nm C_{60} domains still are likely to reach the D–A interface as the mean exciton diffusion length in C_{60} is determined to 8–40 nm [30,31].

In summary, our study demonstrates that EFTEM spectrum imaging is capable of distinguishing the chemistry of a phase separated organic cell absorber based on ZnPc and C_{60} on the sub-10 nm scale. Contrast for the mapping is provided by the fact that the plasmon position in ZnPc/C_{60} composites shifts with increasing C_{60} fraction from 23 to 26 eV. The plasmon map visualizes donor and acceptor phases independently of crystallinity or crystal orientation and therefore allows analyzing their complete lateral phase distribution. The same approach can be applied to characterize and optimize the nanomorphology of any donor–acceptor composites if the constituents provide sufficient difference in their plasmon positions.

Acknowledgements

The authors thank Bernhard Schaffer at SuperSTEM, Daresbury for fruitful discussions. This work was partially funded by the BMBF (joint research project ‘SOHyb’ contract number 03X3525A).

References

[1] M.A. Green, K. Emery, Y. Hishikawa, W. Warta, Solar cell efficiency tables (version 37), Prog. Photovolt: Res. Appl. 19 (2011) 84–92.
[2] M. Vogel, J. Strotmann, B. Johnev, M. Lux-Steiner, K. Fostiropoulos, Influence of nanoscale morphology in small molecule organic solar cells, Thin Solid Films 511–512 (2006) 367–370.
[3] K. Fostiropoulos, W. Schindler, Donor–acceptor nanocomposite structures for organic photovoltaic applications, Phys. Status Solidi. B 246 (2009) 2840–2843.
[4] A.F. Bartelt, C. Strothkämper, W. Schindler, K. Fostiropoulos, R. Eichberger, Morphology effects on charge generation and recombination dynamics at ZnPc:C_{60} bulk hetero-junctions using time-resolved terahertz spectroscopy, Appl. Phys. Lett. 99 (2011) 143304.
[5] P. Peumans, S. Uchida, S.R. Forrest, Efficient bulk heterojunction photovoltaic cells using small-molecular-weight organic thin films, Nature 425 (2003) 158–162.
[6] K. Suemori, T. Miyata, M. Hiramoto, M. Yokoyama, Enhanced photovoltaic performance in fullerene:phthalocyanine codeposited films deposited on heated substrate, Jpn. J. Appl. Phys. 43 (2004) L1014–L1016.
[7] S. Pfuetzner, J. Meiss, A. Petrich, M. Riede, K. Leo, Thick C_{60}:ZnPc bulk heterojunction solar cells with improved performance by film deposition on heated substrates, Appl. Phys. Lett. 94 (2009) 253303.
[8] C.R. McNeill, B. Watts, L. Thomsen, W.J. Belcher, A.L.D. Kilcoyne, N.C. Greenham, P.C. Dastoor, X-ray spectromicroscopy of polymer/fullerene composites: quantitative chemical mapping, Small 2 (2006) 1432–1435.
[9] H. Hoppe, T. Glatzel, M. Niggemann, A. Hinsch, M. Lux-Steiner, N.S. Sariciftci, Kelvin probe force microscopy study on conjugated polymer/fullerene bulk heterojunction organic solar cells, Nano Lett. 5 (2005) 269–274.
[10] E.J. Spadafora, R. Demadrille, B. Ratier, B. Grévin, Imaging the carrier photogeneration in nanoscale phase segregated organic heterojunctions by Kelvin probe force microscopy, Nano Lett. 10 (2010) 3337–3342.
[11] S.S. Bavel, E. Sourty, G. With, J. Loos, Three-dimensional nanoscale organization of bulk heterojunction polymer solar cells, Nano Lett. 9 (2009) 507–513.
[12] B.V. Andersson, A. Herland, S. Masich, O. Inganäs, Imaging of the 3D nanostructure of a polymer solar cell by electron tomography, Nano Lett. 9 (2009) 853–855.
[13] P. Simon, B. Maennig, H. Lichte, Conventional electron microscopy and electron holography of organic solar cells, Adv. Funct. Mater. 14 (2004) 669–676.
[14] J. Hunt, M. Disko, S. Behal, R. Leapman, Electron energy-loss chemical imaging of polymer phases, Ultramicroscopy 58 (1995) 55–64.
[15] R.F. Egerton, Electron energy-loss spectroscopy in the TEM, Rep. Prog. Phys. 72 (2009) 016502.
[16] H. Daniels, R. Brydson, A. Brown, B. Rand, Quantitative valence plasmon mapping in the TEM: viewing physical properties at the nanoscale, Ultramicroscopy 96 (2003) 547–558.
[17] M.H. Gass, K.K.K. Koziol, A.H. Windle, P.A. Midgley, Four-dimensional spectral tomography of carbonaceous nanocomposites, Nano Lett. 6 (2006) 376–379.
[18] A.A. Herzing, L.J. Richter, I.M. Anderson, 3D nanoscale characterization of thin-film organic photovoltaic device structures via spectroscopic contrast in the TEM, J. Phys. Chem. C 114 (2010) 17501–17508.
[19] M. Pfannmöller, H. Flügge, G. Benner, I. Wacker, C. Sommer, M. Hanselmann, S. Schmale, H. Schmidt, F.A. Hamprecht, T. Rabe, W. Kowalsky, R.R. Schröder, Visualizing a homogeneous blend in bulk heterojunction polymer solar cells by analytical electron microscopy, Nano Lett. 11 (2011) 3099–3107.
[20] S. Hashimoto, S. Isoda, H. Kurata, G. Lieser, T. Kobayashi, Molecular orientation of perfluoro-vanadyl-phthalocyanine examined by electron energy loss spectroscopy, J. Porphyrins Phthalocyanines 3 (1999) 585–591.
[21] W. Sigle, S. Krämer, V. Varshney, A. Zern, U. Eigenthaler, M. Rühle, Plasmon energy mapping in energy-filtering transmission electron microscopy, Ultramicroscopy 96 (2003) 565–571.
[22] T. Heil, H. Kohl, Optimization of EFTEM image acquisition by using elastically filtered images for drift correction, Ultramicroscopy 110 (2010) 745–750.
[23] E. Sohmen, J. Fink, W. Krätschmer, Electron energy-loss spectroscopy studies on C_{60} and C_{70} fullerite, Z. Phys. B Condens. Matter 86 (1992) 87–92.
[24] K. Flatz, M. Grobosch, M. Knupfer, The dielectric function of potassium-doped zinc-phthalocyanine, Appl. Phys. A: Mater. Sci. Process. 90 (2008) 243–246.
[25] Y. Saito, H. Shinohara, A. Ohshita, Bulk plasmons in solid C_{60}, Jpn. J. Appl. Phys. 30 (1991) L1068–L1070.
[26] A.E. Porter, M. Gass, K. Muller, J.N. Skepper, P. Midgley, M. Welland, Visualizing the uptake of C_{60} to the cytoplasm and nucleus of human monocyte-derived macrophage cells using energy-filtered transmission electron microscopy and electron tomography, Environ. Sci. Technol. 41 (2007) 3012–3017.
[27] R.F. Egerton, S. Lazar, M. Libera, Delocalized radiation damage in polymers, Micron 43 (2012) 2–7.
[28] J.W. Keller, M.A. Coplan, Electron energy loss spectroscopy of C_{60}, Chem. Phys. Lett. 193 (1992) 89–92.
[29] K. Xun, J. Deng, J. Yao, F. Liu, X. Tao, S. Lü, Z. Wang, S. Wu, Plasmon excitation in 2D and 3D C_{60} studied by photoemission, Chin. Phys. Lett. 10 (1993) 167.
[30] L.A.A. Pettersson, L.S. Roman, O. Inganäs, Modeling photocurrent action spectra of photovoltaic devices based on organic thin films, J. Appl. Phys. 86 (1999) 487.
[31] P. Peumans, A. Yakimov, S.R. Forrest, Small molecular weight organic thin-film photodetectors and solar cells, J. Appl. Phys. 93 (2003) 3693–3723.